Towards Bedmap Himalayas: a new airborne glacier thickness survey in Khumbu Himal, Nepal.

Hamish D. Pritchard[1], Edward C. King[1], David J. Goodger[1], Douglas Boyle[1,2], Daniel N. Goldberg[3], Beatriz Recinos[3], Andrew Orr[1], Dhananjay Regmi[4]

[1]British Antarctic Survey, Cambridge, CB3 0ET, UK
[2]University of Cambridge, UK
[3]School of GeoSciences, University of Edinburgh, UK
[4]Himalayan Research Centre, Kathmandu, Nepal

Correspondence to: Hamish D. Pritchard (hprit@bas.ac.uk)

Abstract

Mountain glaciers provide an important service in sustaining river flows for large populations downstream of High Mountain Asia (HMA) but these glaciers are retreating and the future of this water resource is highly uncertain. Glacier thickness measurements are vital for accurate mapping of the remaining ice reserve and for predicting where and how fast it will decline under climate change, but such measurements are severely lacking in this region due to the difficulties of surveying in remote, high-altitude settings. We report on a uniquely extensive new thickness dataset for eleven glaciers in the Khumbu Himal around Mount Everest that we collected in late 2019 using a novel, low-frequency helicopter-borne radar. To aid in interpreting the survey radargrams we developed a terrain clutter model, and we succeeded in mapping ice thickness with a precision of around ±7 % and horizontal spacing of around 40 m, for thicknesses of up to 445 m and spanning a total of 119 line-km, approximately doubling the length of previous thickness surveys in HMA. To demonstrate the utility of our new measurements, we compare them to existing modelled thickness products and find that the models struggle to reproduce the distribution of ice in these complex, steep, rapidly slowing, thinning and stagnating glaciers, with widespread systematic thin and thick biases equivalent to around half of the measured ice thickness or more. This new dataset (https://doi.org/10.5285/e39647f5-fb72-4d16-acbd-9784ed2167b8) permits for the first time a detailed analysis of model performance on Himalayan glaciers, a key step in improving model skill and hence the accuracy of modelled thickness distributions and future ice loss on the mountain-range scale.

Short summary

We present a new and uniquely extensive dataset of glacier thickness from the Khumbu Himal around Mount Everest that stretches for 119 km, doubling the extent of thickness measurements in High Mountain Asia. Such measurements are key inputs for models that estimate how much ice is stored on the whole mountain range scale and for models that predict how this ice reserve will change in future, and what impact this will have on water supply for the large populations living downstream.

1 Introduction

High Mountain Asia (HMA) contains ~95,000 glaciers which provide an important service in sustaining river flow in the region's relatively warm and dry spring and autumn months, and particularly during droughts

(Pritchard 2019). As many of these glaciers are retreating due to climate change (Maurer, Schaefer et al. 2019), major rivers including the Ganges, Indus and Brahmaputra are in the process of losing the protective hydrological buffer that their glacio-pluvial regimes provide. Large-scale mass balance modelling studies project that roughly half of the glacier ice in HMA (approximately 5,000 km^3, enough to raise sea levels by over a centimetre (Huss and Farinotti 2012)) will be lost by 2100 but there is considerable uncertainty in these projections (Marzeion, Hock et al. 2020, Rounce, Hock et al. 2020). This is in part due to uncertainty in future climate, but uncertainty in the glacier models themselves can match or exceed this climate uncertainty (Marzeion, Hock et al. 2020) for reasons that are intimately connected to a lack of ice thickness measurements (Li, Maussion et al. 2023).

Field surveys of ice thickness are sparse and insufficient on their own for mapping ice distribution beyond the local scale of the survey (e.g., Pritchard 2021), but in several ways they are of key importance to modelled estimates of regional and global ice distribution (Millan, Mouginot et al. 2022) and projections of how this will evolve. In some simpler glacier models, thickness measurements are, for example, used to estimate the spatially distributed thickness distribution through empirical scaling relationships between glacier area, length and volume (Marzeion, Hock et al. 2020, Rounce, Hock et al. 2020). In more sophisticated dynamic ice flow models, they are used to constrain model properties such as ice stiffness and bed friction (e.g., Millan, Mouginot et al. 2022), and such dynamic models have been employed to map regional and global ice thickness distribution through inversion of satellite-derived surface flow (Farinotti, Huss et al. 2019, Millan, Mouginot et al. 2022). These distributions have, however, been prone to large biases (Farinotti, Huss et al. 2019, Pritchard, King et al. 2020, Farinotti, Brinkerhoff et al. 2021, Millan, Mouginot et al. 2022).

Adding to this challenge to mapping the ice thickness distribution, the accuracy of forward modelling projections of glacier retreat under future climate change scenarios is also dependent on thickness-constrained model properties such as ice stiffness and bed friction, and on initial glacier extents, and thickness measurements are critical for refining these extents. Recent studies in HMA have shown that variations in extent between different inventories can cause significant differences in both present-day ice thickness estimates and future mass loss projections, which can be even more sensitive to these inventory choices than to differences in climate forcing scenarios (Li, Maussion et al. 2023). More broadly, model initialisation errors relating to ice thickness cause spurious thinning and thickening patterns, biasing projections of mass change for decades or longer, and in HMA such initialisation uncertainty accounts for 50 % of overall glacier projection uncertainty in the first few decades of simulation (2020-2040) (Marzeion, Hock et al. 2020).

The assimilation of even limited measurements through calibrated inverse modelling techniques can markedly improve the accuracy of modelled projections of glacier retreat and loss, hence spatially distributed glacier thickness surveys are vital (Frey, Machguth et al. 2014, Farinotti, Huss et al. 2019, Maussion, Butenko et al. 2019, Marzeion, Hock et al. 2020, Jouvet and Cordonnier 2023), (Farinotti, Huss et al. 2019, Millan, Mouginot et al. 2022, Li, Maussion et al. 2023), particularly where the measurements sample the thickest parts of the target glaciers and not only the more accessible but typically thinner lower glacier elevations (Farinotti, Brinkerhoff et al. 2021). The profound lack of such measurements in HMA (Pritchard, King et al. 2020, Pritchard 2021) therefore

remains a key barrier to creating an accurate inventory of the region's current ice reserve, and to forecasting how this will change.

80

Ice thickness data are scarce primarily because they are difficult to obtain, even for individual HMA glaciers. Radar or seismic field surveys on the ground are hindered by the practical challenges of working on glaciers that are remote and lie at high altitude, are often very rough, debris-covered and crevassed, and are frequently struck by avalanches and rock falls from surrounding mountain slopes (e.g., Pritchard, King et al. 2020). Airborne radar surveys by fixed-wing aircraft (commonly employed to measure the thickness of the polar ice sheets (e.g., Plewes and Hubbard 2001)) are hindered by a lack of manoeuvrability at high altitude, within the region's narrow and deeply incised glacial valleys. Furthermore, radar signal-penetration is hampered by the high water and debris content of the lower tongues of HMA glaciers (e.g., Macheret, Moskalevsky et al. 1993, Gades, Conway et al. 2000).

90

To overcome the practical challenges of surveying HMA glaciers, Pritchard, King et al. (2020) adapted a low-frequency ice-penetrating radar, developed originally for Antarctic over-snow surveys, for deployment by helicopter in areas characterised by thick, dirty, temperate ice. The light, portable, modular, low-frequency design of the Bedmap Himalayas radar platform, combined with the manoeuvrability of helicopters, make this approach particularly well suited to surveying the remote and otherwise largely inaccessible high-mountain glaciers of this region. Here, we report on the first Himalayan survey with this platform, and the new glacier thickness dataset resulting from it.

2 Methods

2.1 Airborne radar survey

2.1.1 Radar system

We used a wide band mono-pulse dipole radar with a transmitter that produces ± 2000 V pulses at a centre frequency of 7 MHz (Pritchard, King et al. 2020) for this survey. The transmitter, receiving system, antennas and GPS were all mounted on a 24 m long semi-flexible, modular box-section structure built of polyester fibreglass tubing and non-metallic connectors, designed to be flown as a helicopter sling load (Figure 1). We employed transmit and receive antennas each 20 m in overall length, comprising a pair of 10 m half-dipoles with resistor loading to suppress resonance. The antennas overlapped for 80 % of their length and were separated horizontally by 0.7m. This configuration kept the peak voltage entering the digitiser front-end below the overload limit but precluded the use of any amplification stage.
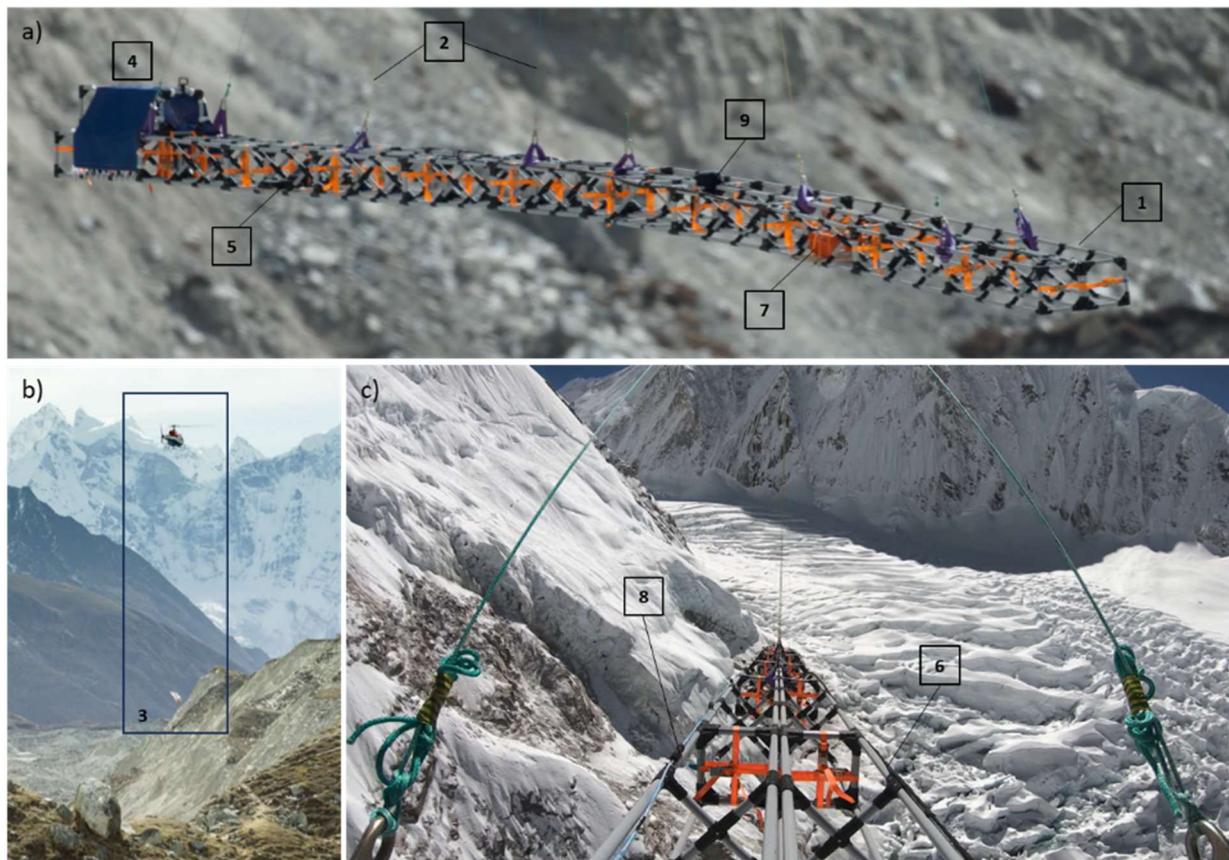
Figure 1 | The radar frame consisting of lightweight fibreglass modules strapped together (1), with rope lines (2) to suspend the system under the helicopter (3), a tail (4) to prevent 'weathercocking', a pulse transmitter (5) and corresponding, resistively loaded transmit dipole antenna (6), receiver (7) and receive antenna (8) and GPS (9) (Pritchard, King et al. 2020). Panel (c) shows the system approaching the icefall on Khumbu Glacier (Figure 2), with multiple potential sources of radar clutter notably from the surrounding mountains and crevasse walls. Photo credits: Hamish Pritchard.

2.1.2 Airborne survey

From 2019-10-27 through 2019-11-06, we deployed our radar platform to survey the glaciers of Nepal's Khumbu Himal (Everest area) in the upper Dudh Koshi river basin, an area notable for holding some of the region's largest glaciers and highest accumulation areas (Figure 2). Porters transported on foot the fibreglass modules, rigging and radar components from the airport at Lukla to a small unpaved airstrip immediately above and north of Namche Bazaar, where we assembled the survey platform. From this staging site, we flew a series of test and survey helicopter flights over the glaciers shown in Figure 2 (see also Table A1). We used locally chartered AS350 helicopters and crew capable of high-altitude operations who operated out of Lukla Airport, and our survey flights covered >200 line-km spanning altitudes of 3700 m to 6700 m.

We flew our radar platform as an underslung load that transmitted continuously and required no electronic connection to the helicopter. The only mechanical connection was that between the helicopter sling hook and the platform rigging, a simple configuration that allowed the platform to be lifted and returned to the ground at our

staging site with or without the helicopter landing and which, for safety, allows the pilot to drop the platform in
130   flight if needed (this was unnecessary during our survey).

Based on the findings of Pritchard, King et al. (2020), we designed our survey patterns to include multiple glacier
cross profiles because these are less prone to ambiguity between radar returns from the glacier bed and valley side
walls. Our flightlines typically followed a continuous zig-zag path with crossings spaced at ~800 m over each
135   glacier trunk for the up-glacier survey limb, with these crossings subsequently linked by a central glacier long-
profile on descent. To minimise radar spreading losses, surveys were flown with the radar platform as close as
safely possible to the glacier surface, typically a few metres to tens of metres given the considerable roughness of
the glacier surfaces in this area. Reaching the highest section of the survey (Everest's Western Cwm), however,
required a spiralling rather than direct ascent over the Khumbu Icefall and so achieved multiple glacier crossings
140   at a wider range of ground clearances (Figure 2). To ensure dense radar sampling, we flew these glacier profiles
as slowly as was practicable (typically ~10 m s^{-1} (36 km h^{-1})). Transit flights to and from the glaciers were at
higher speeds of up to ~40 m s^{-1} (140 km h^{-1}). Our platform remained stable in flight and mechanically sound
throughout the mission.
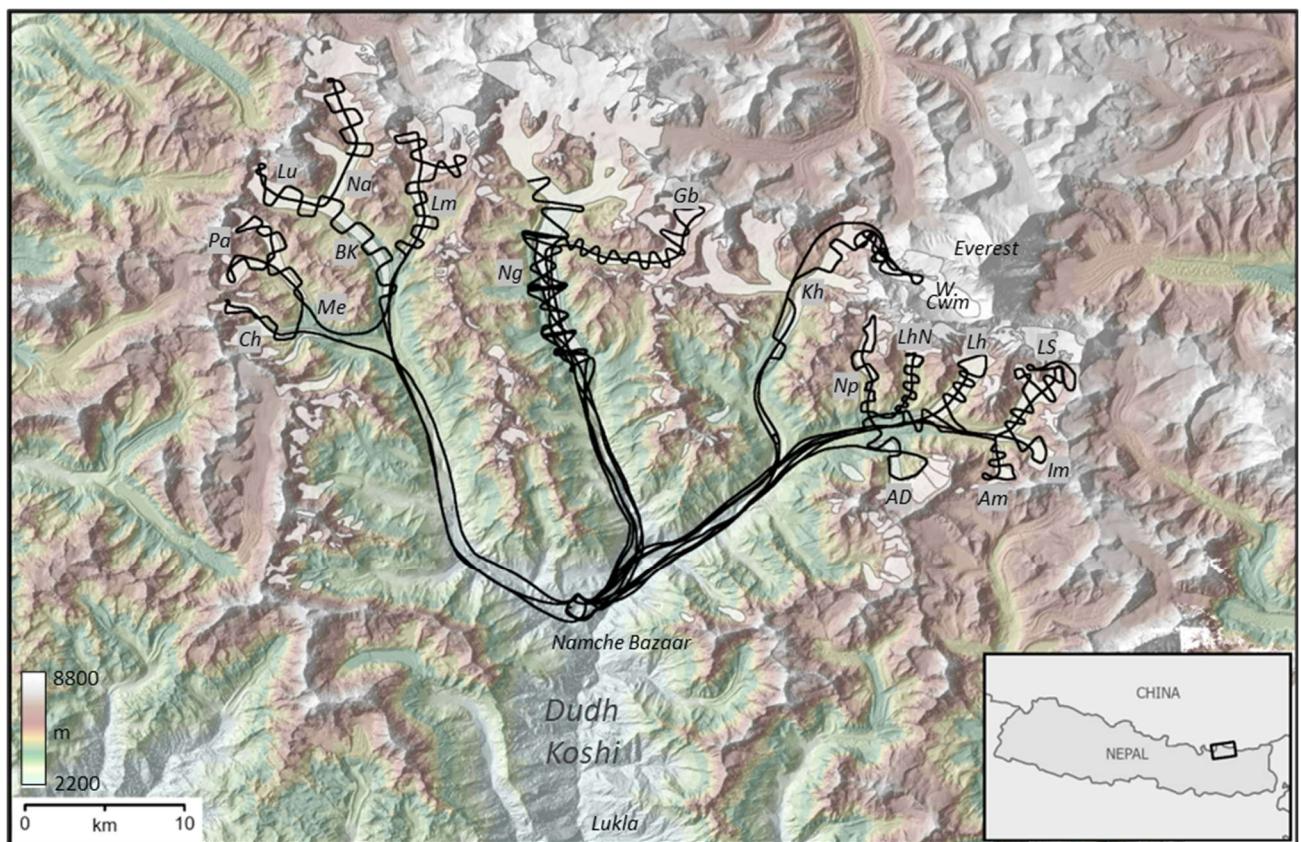
145   **Figure 2 |** Map of the airborne survey (black lines) over the glaciers of the Khumbu Himal, Nepal (white polygons
(RGI Consortium 2017)). Glacier names, after King, Quincey et al. (2017) and Realitymaps.de, are *Ch* = Chhule,
Me = Melung, *Pa* = Pangbug, *BK* = Bhote Kosi, *Lu* = Lunag, *Na* = Nangpa, *Lm* = Lumsamba (Sumna), *Ng* =
Ngozumpa, *Gb* = Gyubanare, *Kh* = Khumbu, *Np* = Nuptse, *Lh = Lhotse, LhN* = Lhotse Nup, *LS* = Lhotse Shar,
Im = Imja, *AD* = Ama Dablam*, Am* = Ambulapcha, *W. Cwm* = Western Cwm of Everest. Background: coloured,
150   shaded-relief topography (Jarvis, Reuter et al. 2008, Shean 2017).

2.2 Data processing

2.2.1 Radar data processing

In processing our radar data, we aimed to produce a set of geometrically correct radargram images from our raw data that we could interpret manually to digitise (pick) profiles of the surfaces and beds of the glaciers, allowing us to quantify the ice thickness. We performed radar processing steps *b-i* using ReflexW version 10.1 software. The key steps were:

a. *Geolocation of the individual traces.* We derived positioning information from dual-frequency GPS units mounted on the suspended radar frame. These were backed up in case of failure by single-frequency GPS data from GoPro cameras also mounted on the frame. The radar traces were time-stamped, so the first processing step was to interpolate GPS positions recorded every second to provide UTM coordinates for each trace on the radargram. We processed the dual frequency GPS data using the online Precise Point Positioning service of the Canadian Geodetic Survey.

b. *Noise suppression through frequency filtering.* Noise arose from within the radar system and from the environment. The main internal noise source was a low frequency radar "wow" component induced in the input stage by the arrival at the radar receiver of the high amplitude spike direct from the transmit antenna. The main environmental noise was relatively low amplitude random noise from HF radio transmissions in the region. To suppress noise, we applied a band-pass frequency filter with a 100 % pass band between 4 and 10 MHz and frequency cut-offs at 2 and 20 MHz.

c. *Amplitude adjustment.* We applied a standard, time-varying amplitude adjustment (divergence compensation) to compensate for the spherical divergence of the propagating radar wave.

d. *Trace interpolation.* We acquired the radar data with a fixed time interval between traces but as the helicopter flight speed was variable, the horizontal spacing between traces also varied. We interpolated the radar data to a fixed horizontal trace spacing as pre-conditioning for the migration step.

e. *Migration*. We employed a finite-difference migration to re-focus hyperbolic returns from point-like scatterers to their origin point. Debris-covered mountain glaciers are a complex of 3D radar targets from along the flightline and from off-axis surface features, subsurface boulders and other irregularities (see Section 2.2.2), but only 2D-migration (along flightline) was possible in this case because our profiles were spaced widely apart to improve survey coverage. Migration of cross profiles was generally more successful than for long profiles at refining the detail of glacier beds, because they tend to traverse the relatively irregular, high relief flanks of glacier bedforms that are otherwise smoothly streamlined in long profile. In the absence of 3D processing, migration was less successful at cleaning the profiles of hyperbolic events arising off to the sides of the flight line from, for example, boulders and surface cliffs. This prompted the need for further declutter processing (Section 2.2.2).

f. *Frequency-wavenumber (fk) filtering to suppress sidewall echoes.* Prominent, diagonally dipping linear reflections are apparent in many cross-profile radargrams, the result of the platform's steady approach towards, and retreat from, steep valley sides and lateral moraine banks to front and rear. Such features have a fixed wave velocity across the record which, when transformed to frequency/wavenumber space, fall in a separate region from horizontal or hyperbolic events. We were able to use this distinction to filter out many such sidewall echoes before transforming the data back to the time/distance domain.

190   g.   *Spatial averaging filter.* As the aim of this survey was to establish the thickness of glaciers in the region, the targets of greatest interest were the spatially continuous beds of the glaciers. To enhance these continuous reflections and suppress random scattering in profiles where the location of the bed was not already clear, we applied a spatial averaging filter.

   h.   *Band-pass frequency filter.* All processing steps tend to introduce noise, so to clarify the profiles we applied a
195   further band-pass filter after all other filtering, with pass band 2-8 MHz and cut offs of 1 and 16 MHz.

   i.   *Geometry correction.* We corrected for variations in altitude of the helicopter and radar platform using the GPS-derived positions and a radar airwave speed of 0.3 m ns^{-1}.

Processing steps *a-h* yielded radargrams like that in Figure 3a, which we used to identify prominent linear
200 reflecting horizons with a form and depth consistent with being the glacier bed. In some cases, we could identify and digitise a single, unambiguous bed horizon, but in other cases, multiple candidate bed horizons were present (e.g., Figure 3b) that required further analysis to distinguish the bed from clutter (Figure 3c and Section 2.2.2). Geometry correction (processing step *i*) then placed the radargram and picked bed in their true geographical context (e.g., Figure 3d).
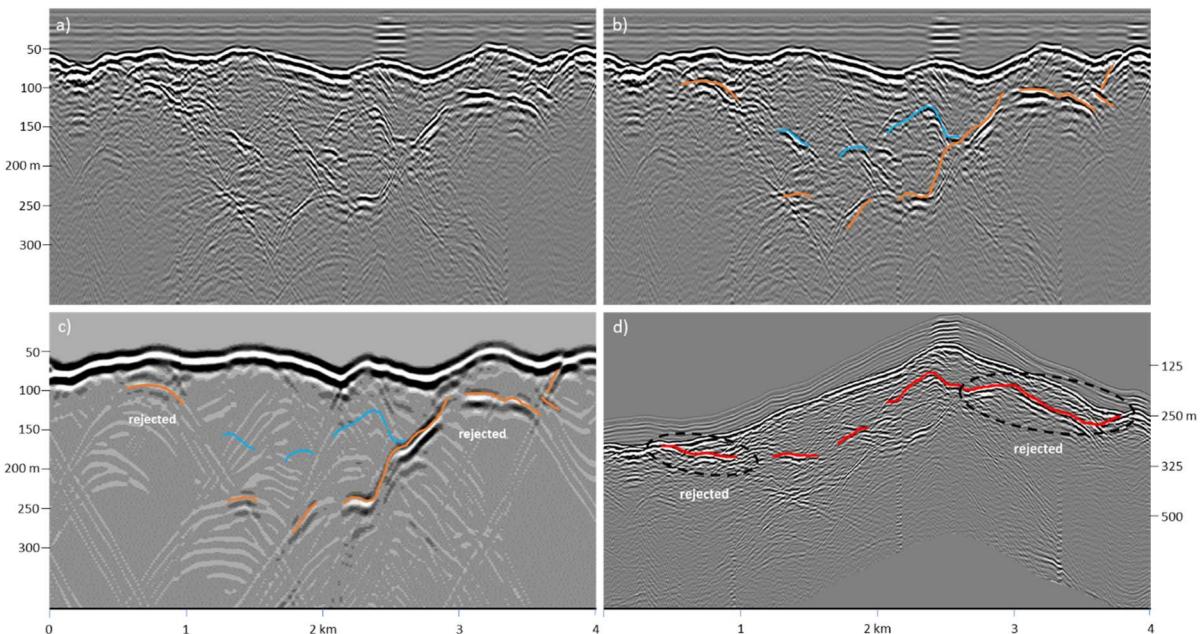
205

Figure 3 | Testing and correction of a manually picked glacier bed using output from the clutter model. a) A survey radargram from Nuptse Glacier, Nepal, with a characteristically complicated set of bright, semi-continuous linear features appearing at various ranges beyond the glacier surface; b) plausible bed picks (orange and blue lines) with ambiguity where they overlap; c) the clutter model for this survey showing that the orange lines
210 correspond to terrain clutter but the blue lines do not, suggesting that the blue lines represent the bed; d) the terrain-corrected radargram with the initial bed pick bed (red lines), highlighting the sections that were subsequently rejected following the clutter test (panel c) (panel d vertical scale differs from other panels) (see also Figure 6).

2.2.2 Clutter modelling

215   The unfocussed, near-isotropic nature of our dipole radar antenna pattern combined with the extreme topographic relief in our survey area and the presence of potentially highly radar-reflective surfaces (such as smooth rock walls, ponds and wet ice cliffs) mean that our survey data contain considerable clutter from the landscape surface, in addition to signals from glacier beds. In particular, the lateral valley walls and moraines of glacier troughs can generate continuous and slowly varying linear features in survey radargrams that are similar to bed signals in form

220   and apparent range (Pritchard, King et al. 2020). Compounding this, signals reflecting from the bed suffer greater attenuation than surface clutter due to radar absorption and scatter by the glacier ice and so are typically weaker. These factors can lead to considerable ambiguity when attempting to pick the bed (Pritchard, King et al. 2020) (e.g., Figure 3b).

225   To help distinguish bed signals from clutter, we developed a clutter model that produces synthetic radargrams based solely on surface scattering, using the survey flightline GPS tracks projected within a digital elevation model (DEM). The clutter model calculates slope and aspect from the DEM and reproduces the range and incidence angle of a spreading radar pulse to all landscape features within radar line of sight (the radar viewshed) from each survey point, outputting the estimated amplitude of the returning signal through time for these features (Figures

230   4, 5). It allows for testing of a variety of surface-scattering models (Lambertian/diffuse reflection, specular reflection, and Minnaert reflection (e.g., Minnaert 1941, Phong 1998), Fig. A1) according to the assumed wavelength-scale roughness of the surfaces encountered, and for testing of variations in the imperfectly-known antenna transmission pattern (from a pulse that is isotropic, to one preferentially directed towards side-lobes perpendicular to the antenna orientation/flightline).

235
    We used this model to approximate the continuously varying surface clutter along each survey flightline, using model parameters that led to the closest visual match to the survey radargrams. We then visually compared the synthetic and real radargrams (e.g., Figures 3a, c) to help distinguish between bed signals and clutter. We manually picked the glacier beds to the best of our ability and used our synthetic clutter radargrams to test these picks, i.e.,

240   to identify 'false beds' that we had misidentified, which we then rejected (e.g., Figure 3d). After this clutter-removal step, we corrected the radargram geometry to account for flying height and speed and projected the geographical locations of the picked bed profiles (e.g., Figure 6).
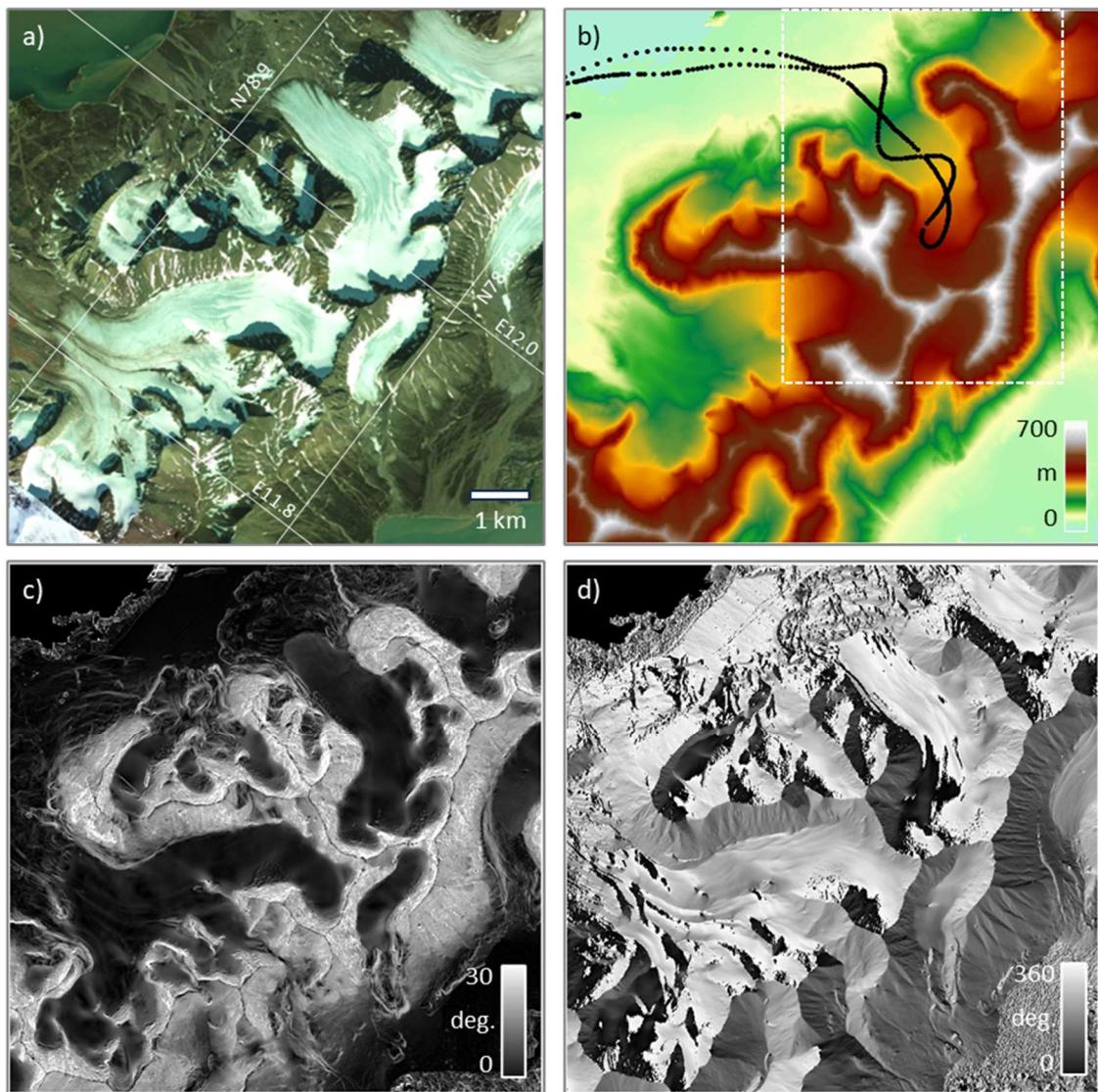
Figure 4 | Example of the terrain properties of a glacial catchment (a) that are used to model clutter, including: b) elevation; c) slope; and d) aspect. The black dotted line in (b) shows a survey flightpath through the landscape (Pritchard, King et al. 2020), the white box shows the area covered in Figure 5.
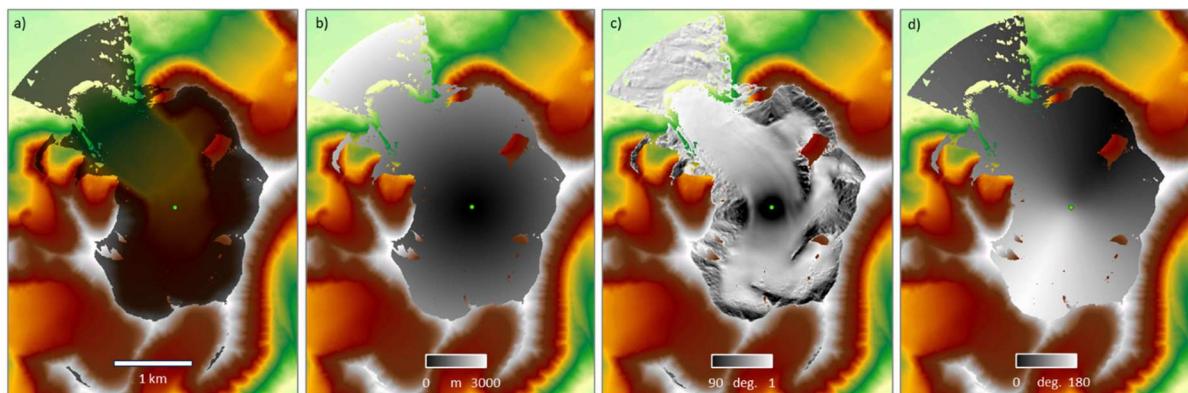
Figure 5 | Terrain analysis for a point (green dot in centre) along the survey flightpath in Figure 4b, including: a) the line of sight viewshed (dark grey mask), and within this viewshed; b) the distance to terrain (greyscale); c) incidence angle of the wavefront meeting the surface (greyscale); and d) directivity angle (flightpath orientation relative to the surface) (greyscale). The background colour scale shows topography as in Figure 4b.
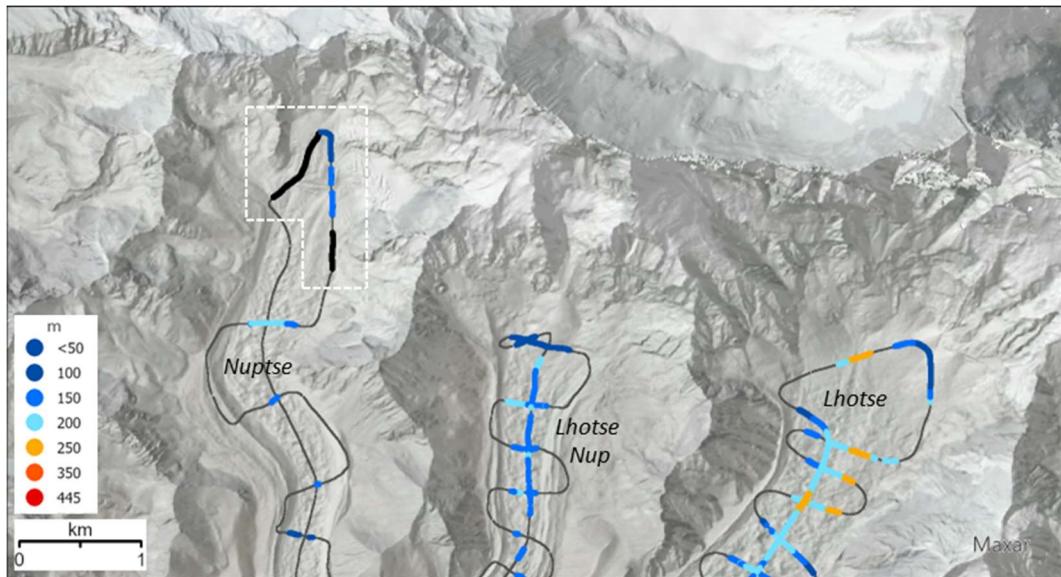
Figure 6 | Flightlines (grey) over Nuptse, Lhotse Nup and Lhotse glaciers, with picked ice thicknesses (colour scale) and mis-picked sections of bed (black) that were rejected following the clutter modelling shown in Figure 3 (sections in white box above). The legend shows the upper value of each thickness class in metres. Background: shaded-relief topography (Jarvis, Reuter et al. 2008, Shean 2017).

3 Results

3.1 Coverage

After data processing, we are able to report ice thickness along a total of 119 line-kilometres in this survey, sampling Khumbu Himal glaciers that cover a total area of 240 km^2 (RGI Consortium 2017) (Figure 7). This is a substantial improvement in our knowledge of glacier thicknesses in this region. There were previously only ~8.4 line-km of thickness data from ground surveys in Khumbu Himal (see Section 3.2) and, more broadly, our ten days of airborne surveying have approximately doubled the combined length of all surveyed profiles from all 95,000 glaciers of HMA collected over the last 60 years, many of which were concentrated on the small (median 2 km^2), thin (mean 52 m) and clean glaciers of the northern HMA, and predate accurate GPS survey-control so have poorly constrained locations (GlaThiDa Consortium 2020).

We measured ice thicknesses of up to 445 m at surface altitudes spanning 4670 m to 6311 m. Our measurements come from a variety of settings, from relatively clean, thin and cold glacier accumulation areas, heavily crevassed icefalls, thick and debris-covered central glacier trunks, and heavily debris-mantled, pond-covered lower glacier tongues (Figure 7). Over the thickest ice we were able to pick the bed only where the glacier surface was relatively clean, in contrast to the debris mantled glacier either side of a clean-ice band (Figure 8), demonstrating the impact of debris cover in limiting radar penetration in such settings.
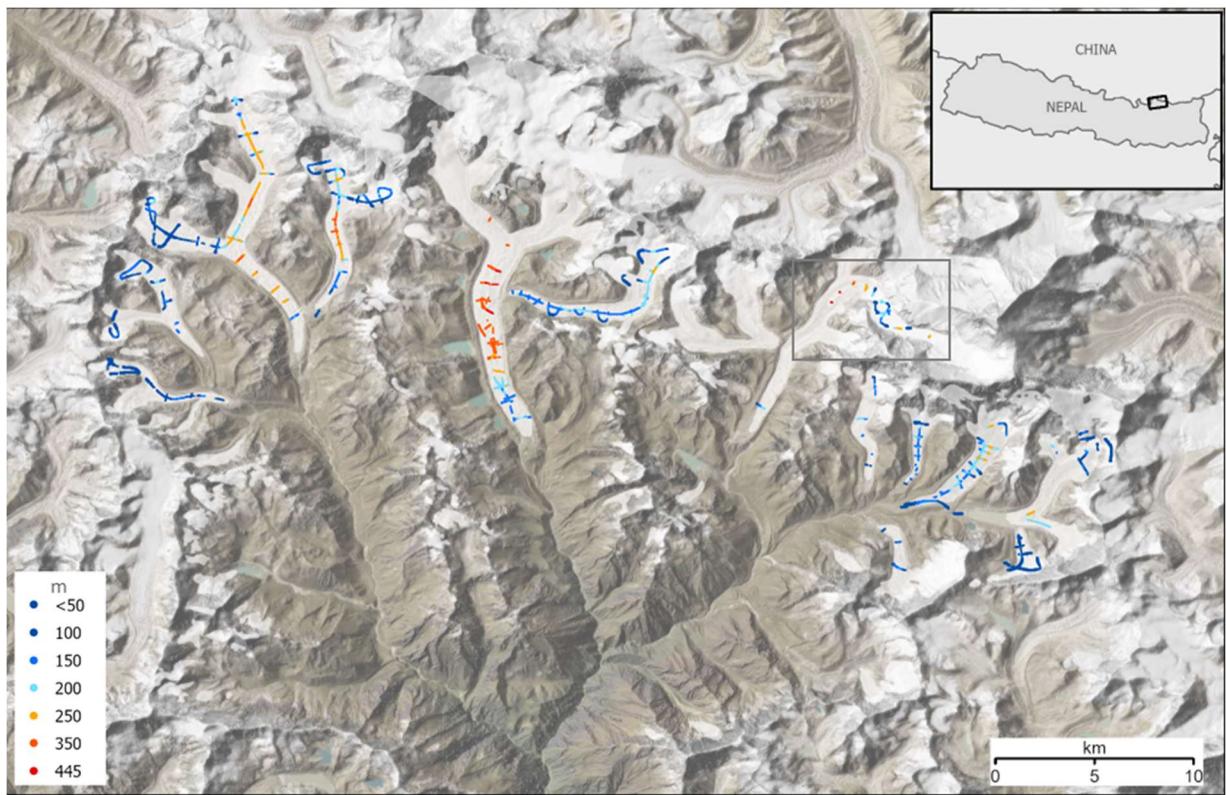
Figure 7 | Ice thickness survey results, with the thickest ice (red) in the central Khumbu Glacier (grey box and Figure 8) followed by central Ngozumpa Glacier (locations in Figure 2). The legend shows the upper value of each thickness class in metres. Background: shaded-relief topography (Jarvis, Reuter et al. 2008, Shean 2017) and glacier extents (RGI Consortium 2017) (white polygons) overlaid on satellite imagery (Earthstar Geographics Undated).
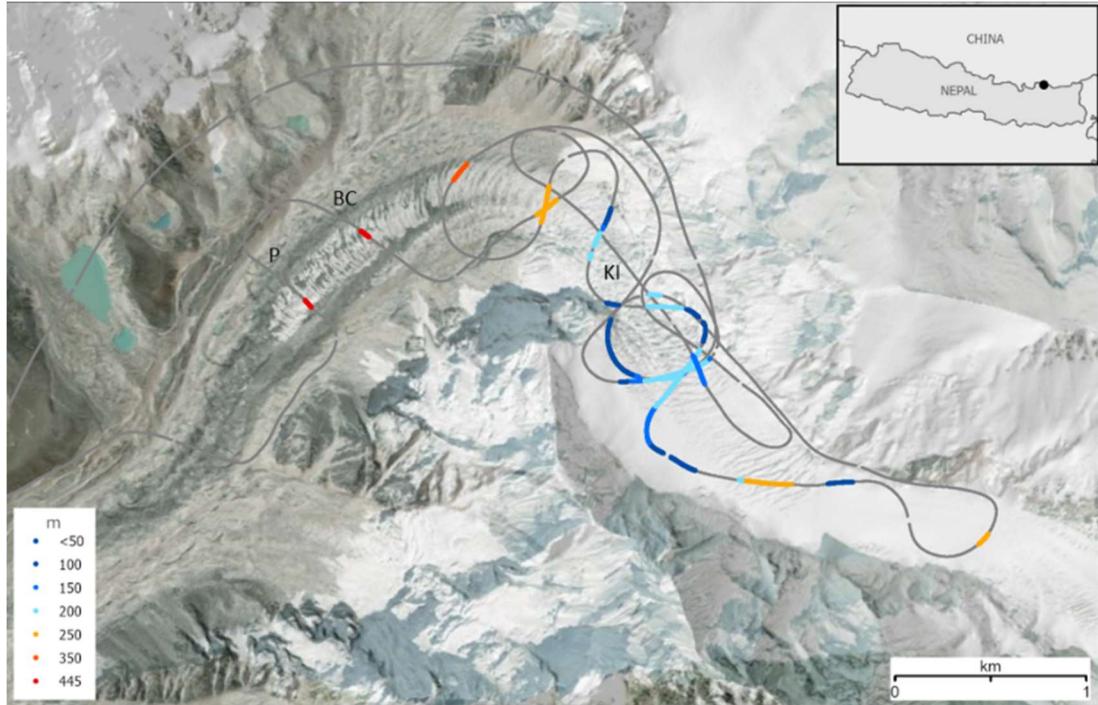
Figure 8 | Successful bed picks on Khumbu Glacier (grey box in Figure 7) showing the thickest ice through which we detected the bed (up to 445 m) in a band of largely clean, debris free ice in the central Khumbu Glacier trunk

285 below the Khumbu Icefall (KI). Note that this coincides closely in location and thickness with radar cross-profiles (in the vicinity of labels P and BC) from a previous ground-based survey (Gades, Conway et al. 2000). Flightlines are shown in grey. The legend shows the upper value of each thickness class in metres. Background: shaded-relief topography (Jarvis, Reuter et al. 2008, Shean 2017) overlaid on satellite imagery (Earthstar Geographics Undated).

Glacier	Survey length (picked bed) (km)	Thickest ice (m)	Mean thickness (SD) (n)	Survey minus Millan mean (SD) (n) (ε)	Survey minus Farinotti mean (SD) (n)	Survey minus Rowan mean (SD) (n)
Chhule	7.08	122	64 (32) (5108)	-27 (41) (4,456) (43)	-10 (24) (4,692)	NA
Melung/Pangbug	6.56	187	95 (39) (5808)	-28 (40) (5,545) (47)	15 (33) (5,699)	NA
Bhote Khosi/Lunag/Nangpa	21.08	292	153 (73) (20940)	4 (49) (20,799) (51)	-20 (59) (20,876)	NA
Lumsamba	15.84	306	146 (69) (15815)	-7 (51) (15,187) (51)	13 (42) (15,323)	NA
Ngozumpa	31.58	384	179 (84) (21618)	-6 (68) (21,091) (57)	0 (68) (21,395)	NA
Khumbu	5.26	445	155 (83) (3051)	-12 (53) (2,795) (55)	50 (63) (2,890)	18 (85) (3040)
Nuptse	1.59	174	129 (36) (1526)	-17 (17) (1,501) (51)	40 (17) (1,511)	NA
Lhotse Nup	3.74	188	121 (40) (2772)	-2 (28) (2,618) (48)	25 (29) (2,667)	NA
Lhotse	13.08	237	137 (49) (9201)	-55 (56) (8,406) (59)	33 (31) (8,554)	NA
Imja/Lhotse Shar/ Ambulapcha	12.44	234	74 (56) (8745)	-12 (44) (6,608) (43)	8 (25) (6,797)	NA
Ama Dablam	0.66	155	105 (25) (1131)	4 (15) (1039) (44)	6 (19) (1,092)	NA
All	**119 km**	**445**	**139 (75) (98,984)**	**-11 (56) (93,304) (52)**	**5 (54) (94,760)**	**NA**

290 **Table 1 |** Ice thickness survey statistics by glacier, and a comparison to previous model results termed 'Millan' (Millan, Mouginot et al. 2022), 'Farinotti' (Farinotti, Huss et al. 2019) and 'Rowan' (Rowan and Egholm 2021), where available (Section 3.3). The difference statistics ('Survey minus Millan', etc) are for all survey points that overlap with these model products, and report the mean difference (m), standard deviation (SD) (m), number of survey points (n) and, in the case of the Millan product, the quoted mean uncertainty for the modelled thickness

295 (ε) (m). (Note that as these statistics refer to the values at the set of points that we successfully surveyed for each glacier (Figure 7): "mean thickness", for example, does not equate to the mean thickness of the entire glacier).

3.2 Resolution, precision, accuracy and validation

With the combination of our 3 kHz radar pulse repetition frequency, the average flying speed while surveying of ~10 m s^{-1} (36 km h^{-1}) and the trace stacking and horizontal interpolation of our data processing, the horizontal

300 sampling in our survey averages 1.15 m (max 3.0 m, SD 0.27 m) along flightlines. However, the horizontal resolution of the bed target is limited by the Fresnel zone (effective radar footprint) of our transmitted pulses. At a frequency of 7 MHz and with the typical range of the glacier bed from the radar (~100-600 m, mean of ~160 m), the Fresnel zone has a radius of approximately 30-80 m (mean ~40 m).

305 In the vertical, the range resolution of the picked surface and bed is nominally a quarter wavelength (~7 m), but the 'optimal vertical resolution' (the resolvable range to a single discrete, prominent reflector (King 2020)) is ~1 m, and the 'practical vertical precision' for such horizons is ~2 m at this frequency (Pritchard, King et al. 2020).

This implies that the practical vertical precision in thickness (assuming that the bed reflector has been correctly identified (see below)) is the combination in quadrature of these two precisions, i.e., ~2.8 m.

310

The absolute accuracy of the thickness is subject to the accuracy of our assumed radar velocity in ice (0.168m ns^{-1}) with which we convert two-way radar travel times to ice thicknesses, and this is somewhat dependent on the unknown and potentially variable depth-averaged glacier water content. A range of velocities from 0.165 to 0.172 m ns^{-1} has, for example, been employed for temperate and cold ice above and below the equilibrium line of an

315 alpine glacier (Macheret, Moskalevsky et al. 1993). This range of velocities implies a difference in ice thickness of approximately ±2 % for our survey (equivalent to a change in mean thickness from 139 m when using a velocity of 0.168 m ns^{-1} to between 137 m and 142 m for the reasonable range of velocities). Given the dependence on water content, this could be manifest as a thickness bias that varies broadly with altitude, with our results potentially too thick by up to 2 % at lower (warmer) altitudes, too thin by up to 2 % at higher (colder) altitudes.

320 Potentially more significant bias (e.g., tens of metres) could result from mistaking a non-bed reflection horizon for the bed, which we sought to avoid with our clutter modelling (Section 2.2.2).

To assess the consistency of our picked thickness measurements, we quantified the difference in thickness at 79 flightline crossovers (Figure 9). The mean absolute crossover difference was 9 m and the mean relative difference was 7 % of thickness (median 6 m and 5 %) (Table 2). We also compared our airborne survey results to previous

325 ground-based radar surveys on Khumbu (Gades, Conway et al. 2000) and Ngozumpa glaciers (Pritchard, King et al. 2020). On Khumbu Glacier, seven radar cross profiles were surveyed in 1999 over the glacier tongue below the Khumbu Icefall, totalling 3.3 km in length (Gades, Conway et al. 2000). Of these, two lines crossed within ~200 m horizontally of two of our successfully surveyed cross profiles (around P and BC in Figure 8). While the earlier ground-based survey achieved profile lengths of ~500 m each, spanning most of the glacier width, we were

330 only able to pick the bed over around 70 m of our profiles at each location. Although these surveys differ in date, method and exact location, the thicknesses reported by both surveys are similar: we measured maximum thicknesses of 445 m close to line P and 440 m close to line BC, compared to maxima of ~370 ± 20 m (line P) and 440 ± 20 m (line BC) in the previous study (Pritchard, King et al. 2020). A thickness of ≤450 ± 70 m close to these lines was also observed by a terrestrial gravity survey in 1976 (Moribayashi 1978).

335
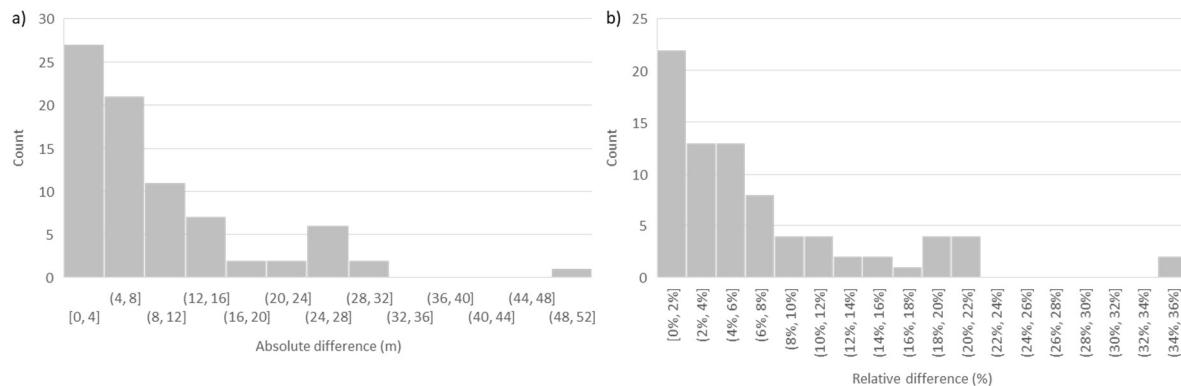
Figure 9 | Frequency distribution of a) absolute and b) relative crossover thickness differences.

Crossover summary	Mean	SD	Median	Max
Relative difference (%)	7	7	5	30
Absolute difference (m)	9	9	6	51

340   **Table 2** | Statistics of surveyed thickness differences measured at 79 flightline crossovers.

On Ngozumpa Glacier, we also compared our airborne survey results to an earlier ground-based radar survey that collected 5.1 line-km of data in 2016 (Pritchard, King et al. 2020). We used the ground survey in some cases to help avoid erroneous bed picks in the airborne survey radargrams, where clutter 'horizons' made bed detection

345   ambiguous, but the thickness distributions of these datasets are otherwise independent. For four zones where both surveys have extensive, though non-identical, coverage (Table 3, Figure 10), this comparison shows close similarity between both the means (-13 m to +8 m difference, with a weighted mean difference of ~0.2 m) and standard deviations (2-7 m difference) of thickness in these zones. The variation in sign of the thickness differences between these datasets suggests that there is no systematic bias between the surveys.

350

In summary, this assessment suggests that our survey data suffer from little systematic bias (typically <2 %) and have a precision that we estimate as around ±7 % of thickness (±10 m for the mean thickness of 136 m). Local inaccuracies can reach ~30 % of ice thickness.

Data source	Mean thickness (m)	Standard Deviation	n	Thickness difference (m)(%)
Zone 1 - ground	345	28	612	0
Zone 1 - air	345	21	578	
Zone 2 - ground	258	13	471	+8 (3 %)
Zone 2 - air	266	15	1727	
Zone 3 - ground	174	15	133	0
Zone 3 -air	174	13	475	
Zone 4 - ground	140	12	262	-13 (10 %)
Zone - air	127	10	996	

355   **Table 3** | Comparison of thickness statistics between samples of ground-based (Pritchard, King et al. 2020) and airborne survey results from zones 1-4 on Ngozumpa Glacier (Figure 10). (Note that we combine the results from this ground survey with those from our airborne survey in our Khumbu Himal thickness dataset (DOI)).
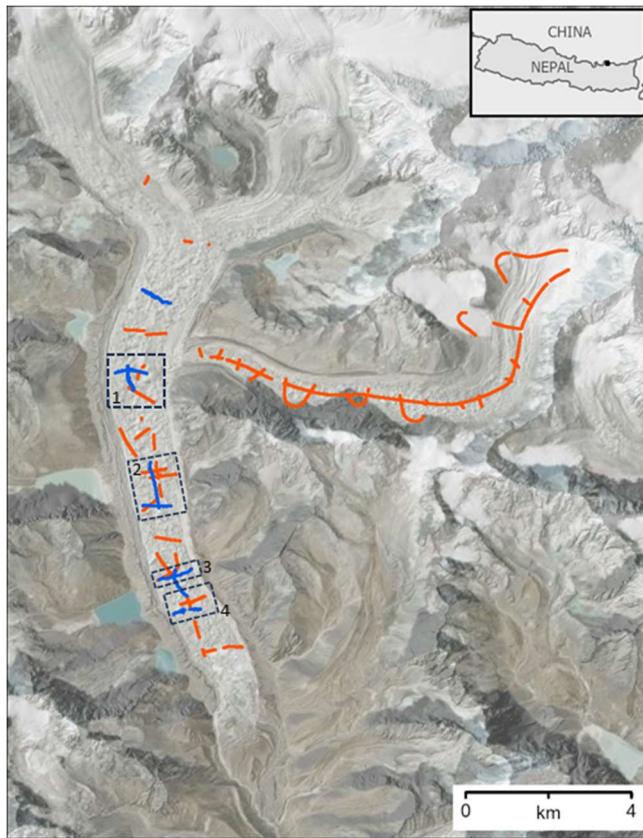
Figure 10 | Boxes 1-4 show the samples of ground-based survey results (blue) and the samples of airborne survey
results (orange) on Ngozumpa Glacier (Table 3). Background: shaded-relief topography (Jarvis, Reuter et al. 2008,
Shean 2017) overlaid on satellite imagery (Earthstar Geographics Undated).

3.3 Comparison to prior modelled thickness estimates

Our main goal in developing our method and conducting this survey was to provide an improved observational
dataset for testing ice thickness models. To demonstrate the utility of our new dataset to the broader glacier
modelling community, we here make an initial, direct assessment of the performance of three existing modelled
thickness products that coincide with our survey dataset:

i)   'Rowan' (Rowan and Egholm 2021, Rowan, Egholm et al. 2021), a thickness grid for Khumbu Glacier
     representing the year 2011 and calculated using a flow law for plastic ice, observed surface slope and
     estimated basal shear stress, modified by a semi-empirical 'shape factor' accounting for the effect of the
     valley sides on ice flow and a down glacier 'thinning factor' to account for non-steady-state mass balance.
     This relationship was tuned using the earlier radar and seismic thickness observations (Moribayashi 1978,
     Gades, Conway et al. 2000) (Section 3.2) and the model was able to reproduce past and present glacier
     extents, present surface elevations and present surface flow rates, but thickness accuracy and precision are
     not reported (Rowan and Egholm 2021).

ii) 'Millan' (Millan, Mouginot et al. 2022), a set of thickness grids for most of the world's glaciers for years
     2017/2018 that employed the shallow-ice-approximation (SIA) to calculate thickness distribution using the
     observed glacier surface slope and flow rate, with region-averaged ice rheology and basal sliding
     parameters estimated through a regional calibration against ice thickness measurements available at that
     time. Accuracy and precision assessed against independent measurements from the Alps were estimated as

380   −16 ± 51 m, or a precision of 25–35 % for ice thickness greater than 100 m, >50 % for ice thicknesses

below 100 m. Limitations ascribed to this model include temporal mismatches between mappings of

velocity (2017-2018), surface slope (2000-2015), glacier extent (2003), and ice thickness (variable dates

and limited extent), and the model was found to perform relatively poorly where the surface slope of the

ice is nearly flat (Millan, Mouginot et al. 2022).

385   iii)   'Farinotti' (Farinotti, Huss et al. 2019), a set of thickness grids for most of the world's glaciers for

approximate years 2000-2010 based on an ensemble of up to five thickness models: a) a mass conservation

approach driven by a regional estimate of the surface mass balance gradient and observed surface slope

and area, with regional flow parameters calibrated using thickness observations where available; b) an

empirical relationship between the altitude range of the glacier and average basal shear stress within

390   altitude zones, modified by an empirical shape factor, with further parameter calibration against available

thickness observations; c) a mass conservation approach driven by gridded climate data (localised rather

than a regional estimate) and observed surface slope using SIA along multiple flowlines, also with flow

parameters calibrated using available thickness observations; d) a mass-conservation and SIA approach

driven by surface mass balance constrained by satellite gravimetry, altimetry and field observations, with

395   flow parameters again calibrated using available thickness observations; e) an alternative version of (b)

above, but with only the shape factor calibrated using thickness observations. Previous tests against

independent ice thickness measurements showed that the consensus thickness grids had negligible bias and

a precision of ±26 % on the regional and global scale, but uncertainties were not provided for individual

glaciers (Farinotti, Huss et al. 2019).

400

As is apparent from the model descriptions above, the accuracy of these gridded ice thickness products is

dependent on the availability, accuracy and representativeness of surveyed thickness measurements which, as

discussed, were particularly poor in this region. Assessed against the full extent of our new survey dataset, we

found on average a small model thick bias (11 m) for Millan and a small thin bias (5 m) for Farinotti (Table 1).

405 Biases are larger for individual glaciers, however, with a glacier-average thick bias of 55 m for Millan on Lhotse

Glacier, and thin biases of 50 m and 18 m on Khumbu Glacier for Farinotti and Rowan respectively (Table 1).

Furthermore, the spatial distribution of thickness biases shows coherent patterns on the sub-glacier scale (Figure

11), some of which are consistent between the models. We find, for example, a thin bias in central Ngozumpa,

central Khumbu, lower Imja and lower Lumsamba glaciers, and a thick bias on lower Ngozumpa, upper Lunag

410 and upper Lumsamba glaciers (locations in Figure 2).
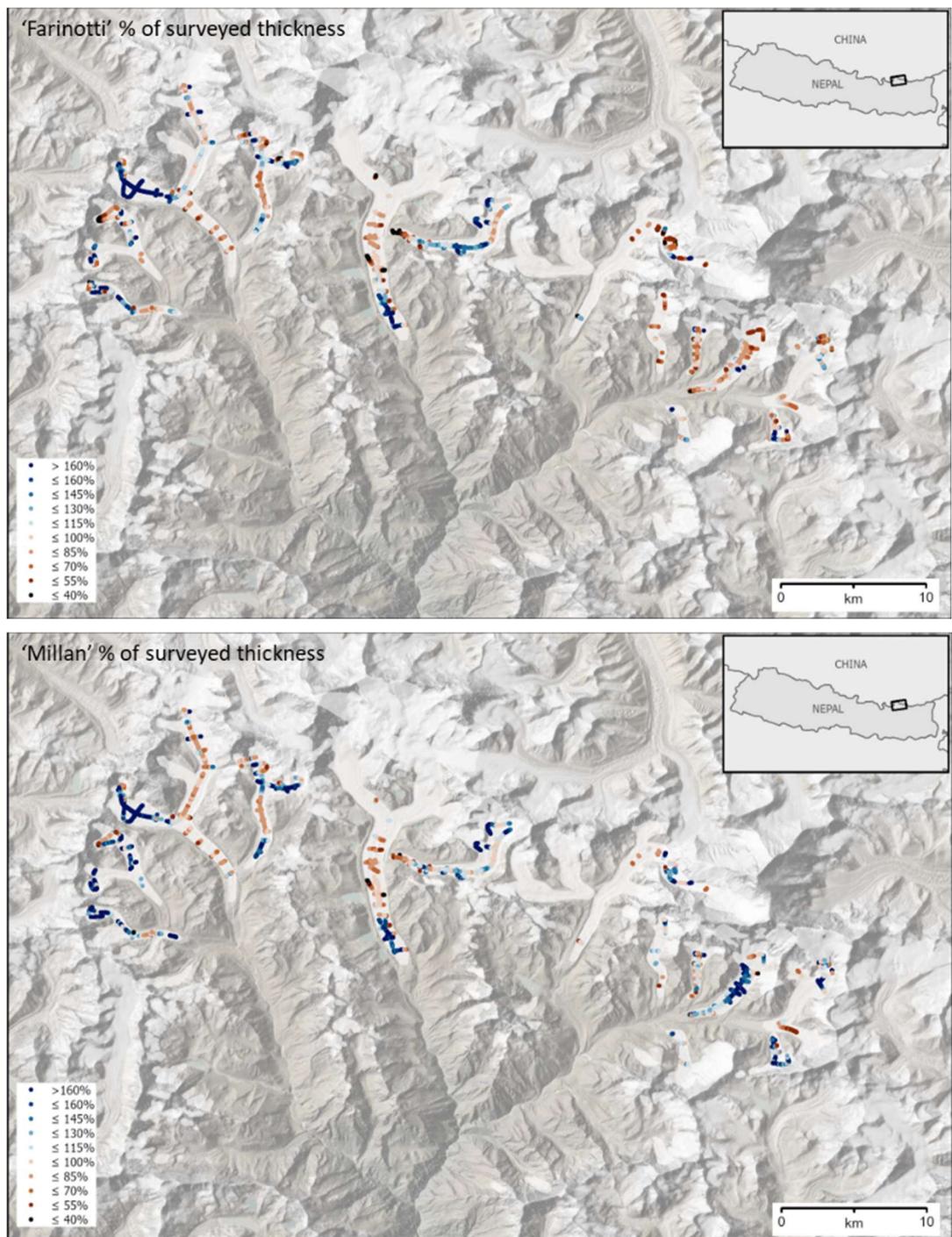
Figure 11 | The spatial distribution of thickness biases in the Farinotti and Millan modelled products. The values shown are modelled thicknesses as a percentage of surveyed thicknesses: blue where the model is too thick, brown where it is too thin. See also Fig. A2 for the spatial distribution of absolute biases in metres. Background: shaded-relief topography (Jarvis, Reuter et al. 2008, Shean 2017) and glacier extents (RGI Consortium 2017) (white polygons) overlaid on satellite imagery (Earthstar Geographics Undated).
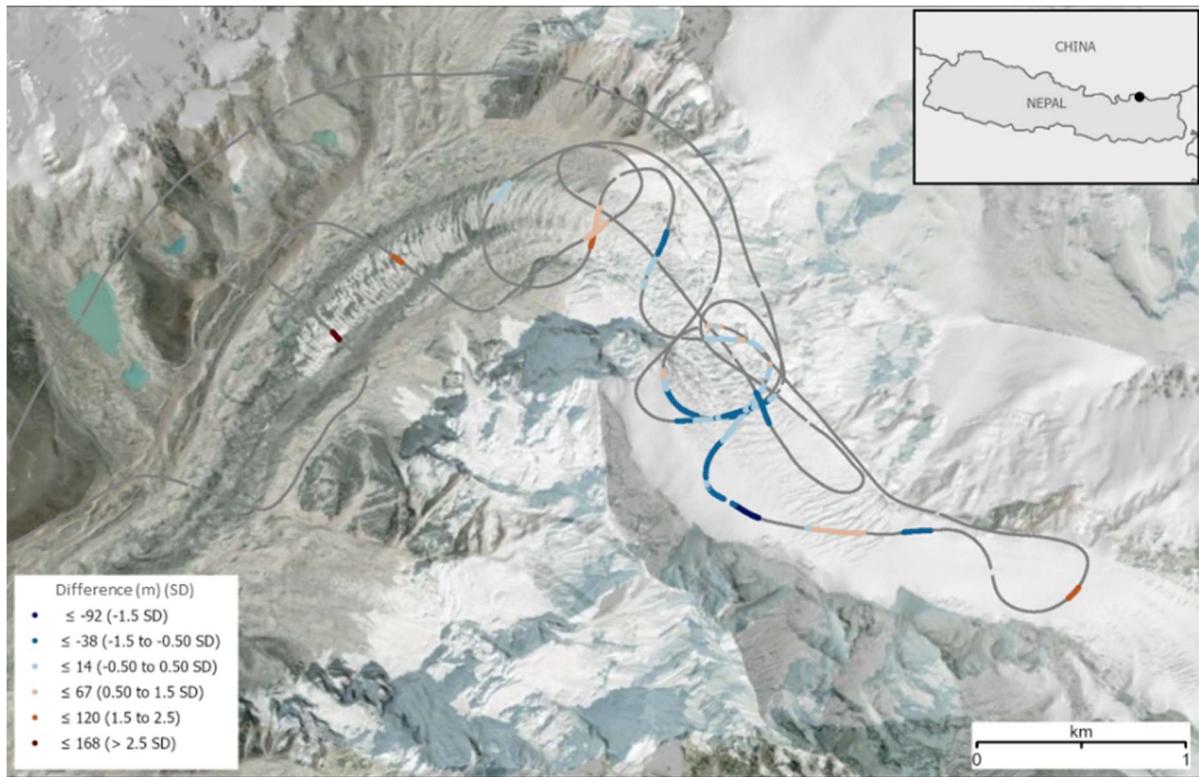
Figure 12 | Surveyed thickness minus modelled Millan thickness (Millan, Mouginot et al. 2022), in metres and in multiples of standard deviations (SD) of difference from the mean difference of -12 m for Khumbu Glacier. Negative (blue) values indicate that the model grid is too thick, positive (brown) values that it is too thin. The largest thin biases in this model tend to correspond with the thickest ice and the largest model thick biases tend to correspond with the thinnest ice (cf. Figure 8). Background: shaded-relief topography (Jarvis, Reuter et al. 2008, Shean 2017) overlaid on satellite imagery (Earthstar Geographics Undated).

The thickness biases for both Farinotti and Millan are somewhat positively correlated (R^2 of 0.301 and 0.373 respectively) with absolute thickness, with both models overestimating the thickness of thin ice and underestimating the thickness of thick ice (Figures 11, 12, 13a). There is little correlation between bias and altitude when assessed over the full altitude range of the measurements, but a stronger correlation (R^2 of 0.376 and 0.407 respectively) for the lowest sections of the glaciers (<4900 m). Specifically, both Millan and Farinotti overestimate the thickness of the lowest-altitude ice (<4800m) while underestimating it in the altitude range 4800-5000 m (e.g., Figure 13b) (though we note that most of our <4800 m survey data come from Ngozumpa Glacier alone (Figure 14)). We find no correlation between model thickness bias and surface slope but, for Farinotti, we find that the gridded product tends to underestimate ice thickness (by a mean of 22 m across this survey) where the glaciers flow relatively fast (>10 m a^{-1}), and where the flow rate has decreased most strongly since the 1980s (by a mean of 39 m thickness for deceleration >1 m a^{-1} dec^{-1}) (Gardner, Fahnestock et al. 2022) (Figures 14, 15). Together, these findings suggest that the models struggle to reproduce ice distribution within such Himalayan glaciers, which have complex geometries, high relief and a wide range of ice thicknesses, are not in steady state, and contain areas of near-stagnant ice in their lower tongues (Figure 14). Further analysis of individual model behaviour is needed to diagnose the causes of model bias that we reveal.
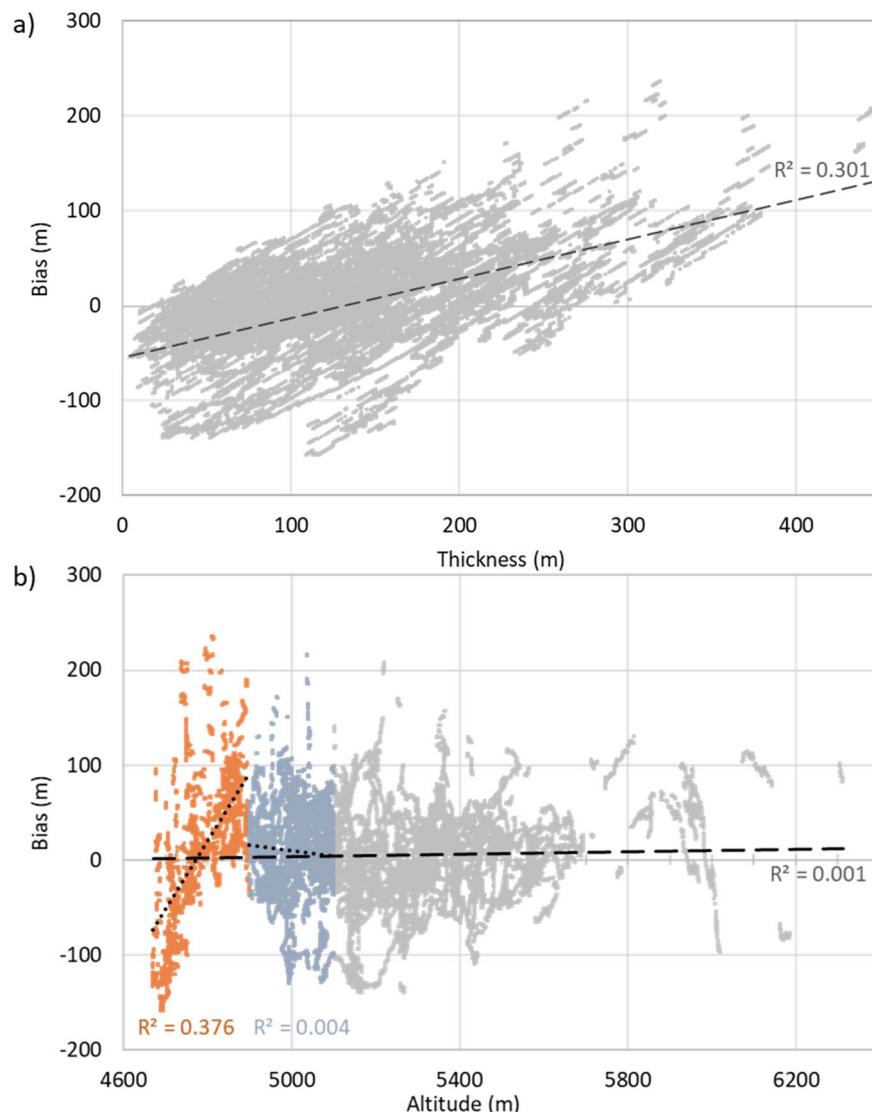
445

Figure 13 | Biases for the Farinotti thickness product plotted against a) absolute thickness, and b) altitude (Shean 2017), with coloured sections highlighting apparent variability in this relationship for different sections of the glaciers (orange = 4700-4900 m, blue = 4900-5100 m). Bias is calculated as surveyed minus modelled thickness (negative indicates that the model is too thick).
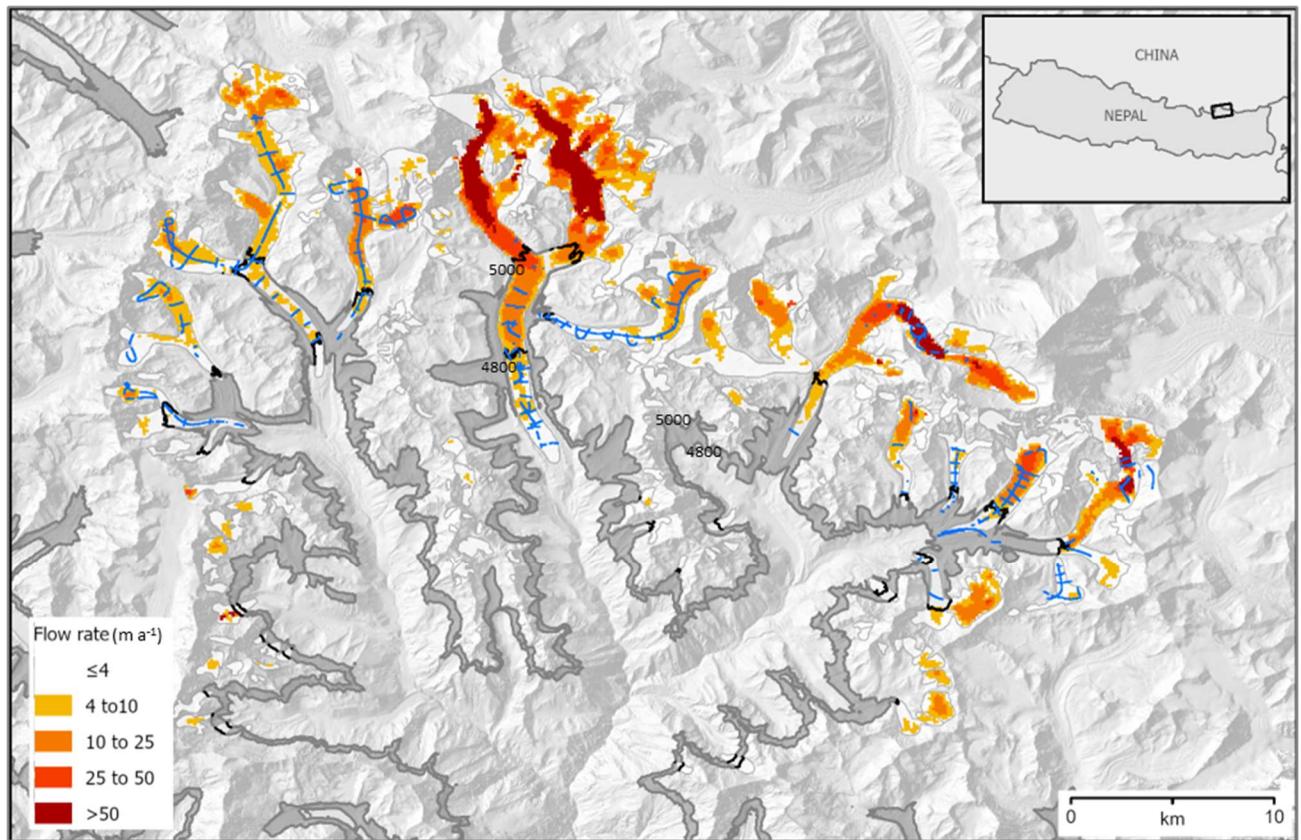
450

Figure 14 | Flow rate (after Gardner, Fahnestock et al. 2022) (colour scale) and extent (white polygons (RGI Consortium 2017)) of glaciers in this study, with the 4800-5000 m altitude band highlighted (grey polygon and black lines where this crosses glaciers) (after Shean 2017). Location of survey data is shown in blue. Background: shaded-relief topography (Jarvis, Reuter et al. 2008, Shean 2017) and glacier extents (RGI Consortium 2017)

455   (white polygons).
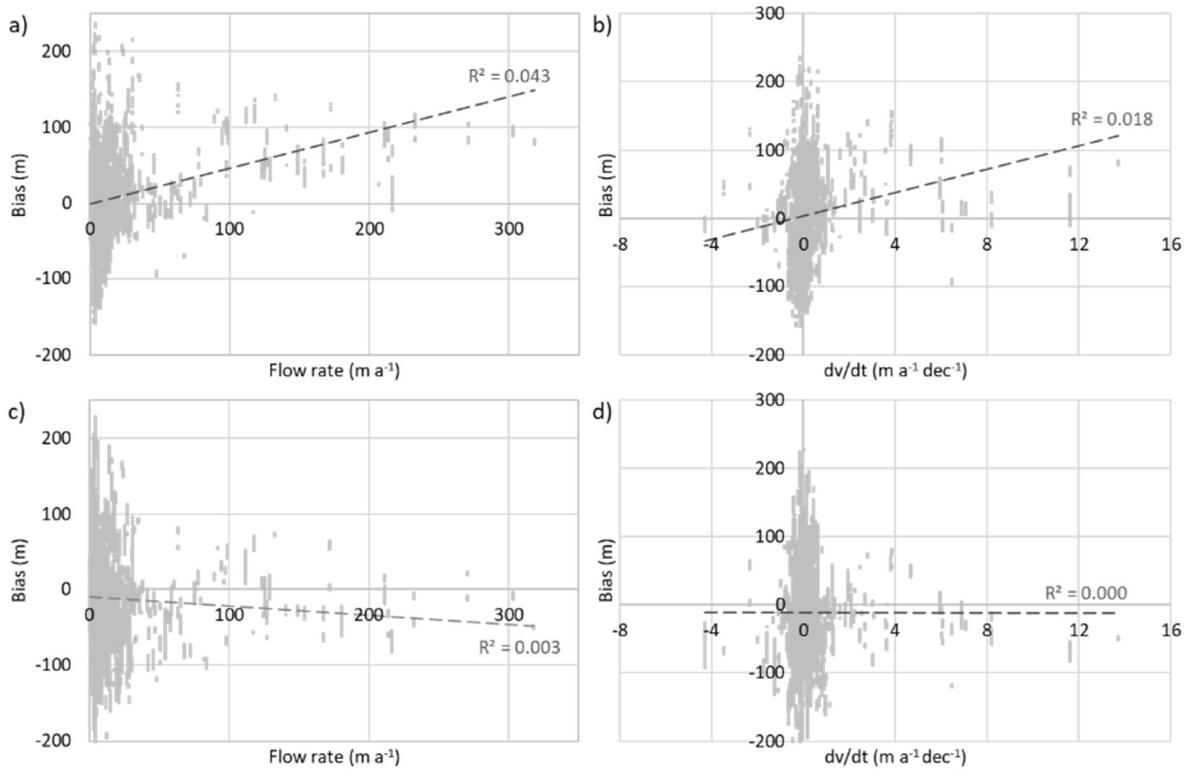
Figure 15 | Farinotti thickness bias against a) flow rate, and b) rate of change in flow (dv/dt in metres per year per decade) (Gardner, Fahnestock et al. 2022); Millan thickness bias against c) flow rate, and d) rate of change in flow.

Data availability

The original and processed radar data and the picked ice thicknesses, along with their metadata, are available from the NERC EDS UK Polar Data Centre: https://doi.org/10.5285/e39647f5-fb72-4d16-acbd-9784ed2167b8 (Pritchard, King et al. 2025).

Code availability

The clutter model code is available here https://zenodo.org/records/15488954 (wiki available at https://github.com/bearecinos/radar-declutter/wiki).

Conclusions

The portability and simplicity of our lightweight but long, modular radar platform proved well suited to helicopter surveys of remote mountain glaciers. We were able to detect the beds and map the thickness of numerous previously unsurveyed stretches of glacier in the Khumbu Himal of Nepal, including the area's largest glacier, Ngozumpa, and possibly it's thickest ice, in Khumbu Glacier, with little bias and a precision of around ±7 %. Data processing for bed detection was challenging primarily due to clutter from the surrounding terrain, but our clutter modelling proved valuable in identifying reflections that did not come from the bed. With this one survey we have doubled the length of thickness survey lines in High Mountain Asia, and our new thickness dataset provides

important insights into the performance of glacier-thickness models. It reveals, for example, that systematic model biases of tens of metres exist for some glaciers, and >100 m (and >100 % of surveyed thickness) for some sub-sections of glaciers, notably in the lower tongues of the glaciers studied. Our new survey capability, and this new survey dataset, allow the strengths and weakness of such models to be examined. This can therefore lead to improved and validated assessments of glacier ice reserves in mountain ranges around the world, and better projections of how they will change in future.

480

Appendix A

Processed flightline segment	Glacier
2019_10_28_F1_P23	Gyubanare (Ngozumpa)
2019_10_30_F1_P64	Ngozumpa
2019_10_30_F1_P74	Ngozumpa
2019_11_03_F1_P32	Lhotse
2019_11_03_F2_P75	Lhotse Shar/Imja/ Ambulapcha
2019_11_04_F1_P24	Lhotse Nup
2019_11_04_F1_P56	Nuptse
2019_11_04_F1_P64	Ama Dablam
2019_11_04_F1_P75	Nuptse
2019_11_04_F1_P85	Lhotse Nup
2019_11_04_F1_P95	Ama Dablam
2019_11_05_F1_P24	Ngozumpa
2019_11_05_F1_P37	Ngozumpa
2019_11_05_F1_P45	Ngozumpa
2019_11_05_F1_P53	Ngozumpa
2019_11_05_F1_P83	Ngozumpa
2019_11_05_F1_P93	Ngozumpa
2019_11_06_F1_P15	Bhote Kosi
2019_11_06_F1_P19	Lunag
2019_11_06_F1_P35	Nangpa
2019_11_06_F1_P39	Lunag
2019_11_06_F1_P45	Nangpa
2019_11_06_F1_P49	Bhote Kosi
2019_11_06_F1_P66	Nangpa
2019_11_06_F1_P77	Nangpa
2019_11_06_F1_P87	Nangpa
2019_11_06_F1_P95	Nangpa
2019_11_06_F1_P98	Nangpa
2019_11_06_F2_P15	Pangbug
2019_11_06_F2_P45	Pangbug
2019_11_06_F2_P54	Lumsamba
2019_11_06_F2_P62	Melung/Pangbug
2019_11_06_F2_P75	Lumsamba
2019_11_06_F2_P83	Lumsamba
2019_11_06_F2_P93	Chhule
2019_11_06_F2_P94	Chhule
2019_11_06_F3_P12	Khumbu
2019_11_06_F3_P69	Khumbu

485 **Table A1** | Table of survey flight details. The flightline names are in the format yyyy_mm_dd_flightnumber
_ProcessingStep and correspond to the processed radargram files (see https://doi.org/10.5285/e39647f5-fb72-
4d16-acbd-9784ed2167b8). The glacier locations are shown in Figure 2.
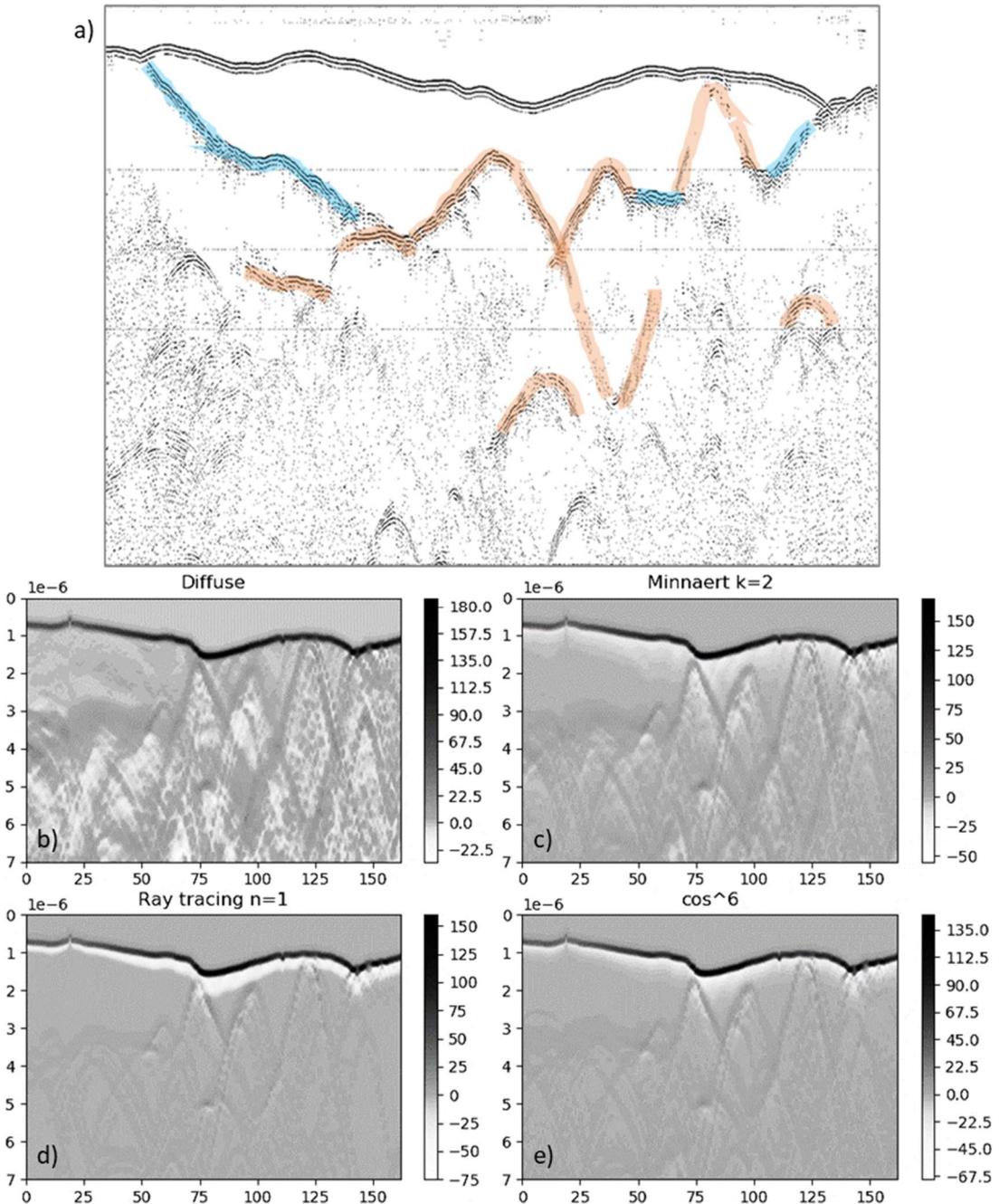
Figure A1 | Testing of scatter models. a) Contrast enhanced survey radargram from the flightline in Figure 4b. (b-e) Modelled clutter using surface-scatter models (e.g., Minnaert 1941, Phong 1998) specified as diffuse, Minnaert (k=2), specular reflection ("Ray tracing") and Minnaert ($\cos^6$) for the same flightline. Blue lines in (a) are bed-like features absent in the modelled clutter in (b), (c), (d) and (e), and so are interpreted as bed. Orange lines in (a) correspond to bed-like features modelled as clutter and so are not picked as bed. Greyscale values show relative signal strength.
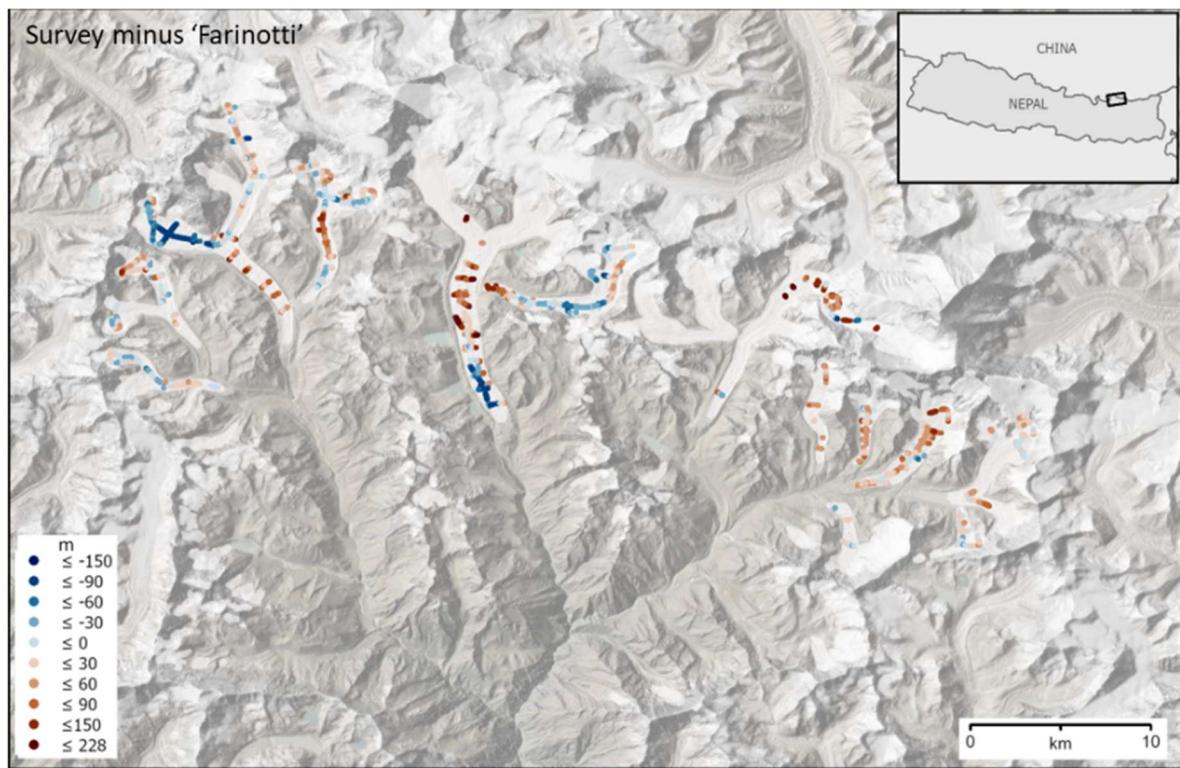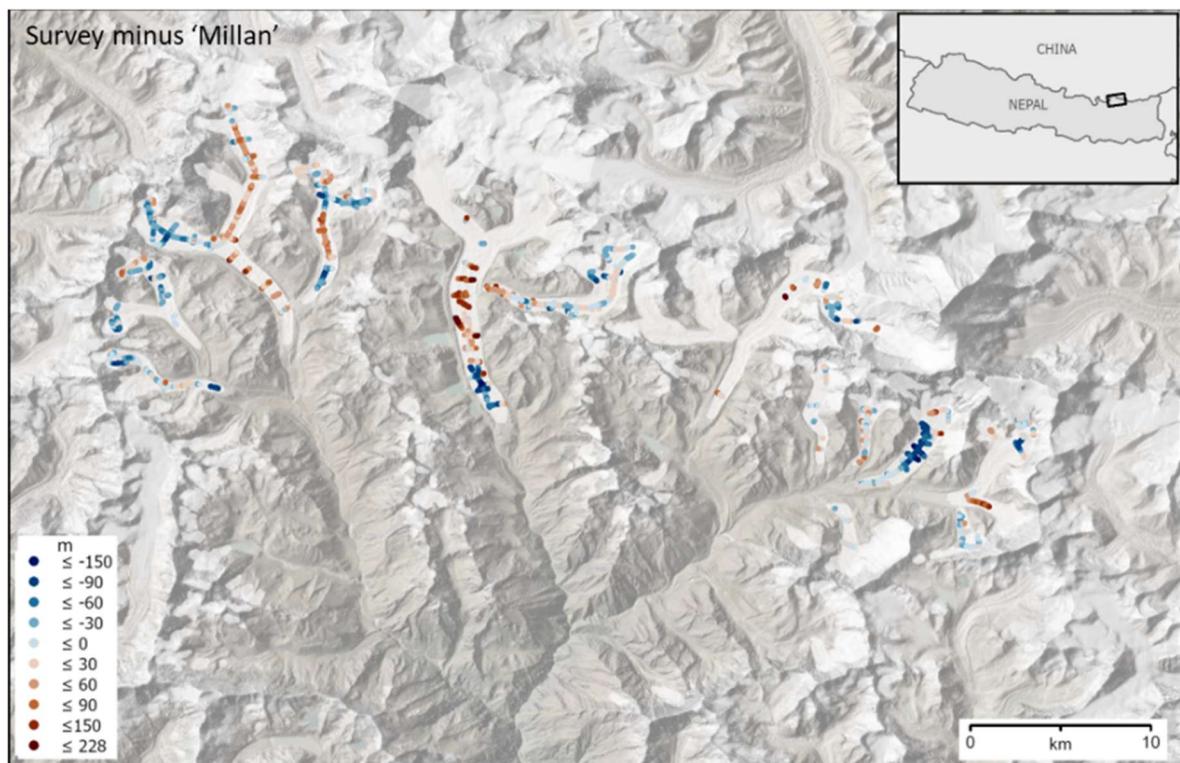
Figure A2 | The spatial distribution of thickness biases (m) in the Farinotti and Millan models. The values shown are survey thicknesses minus model thicknesses, where negative (blue) implies that the model is too thick, positive (brown) that it is too thin. Background: shaded-relief topography (Jarvis, Reuter et al. 2008, Shean 2017) and glacier extents (RGI Consortium 2017) (white polygons) overlaid on satellite imagery (Earthstar Geographics Undated).

Author contribution

HP designed and managed the project and led the field survey and manuscript preparation, EK and HP processed and interpreted the radar data, EK and DG designed and built the radar electronics and software and operated the radar in the field, DB wrote the clutter tool software, DNG and BR updated and implemented the clutter tool, AO supported the survey permitting process and DR supported the field survey design and led the field logistics provision.

Competing interests

The authors declare that they have no conflict of interest.

Acknowledgements

This work was funded by NERC grants NE/X005267/1, NE/R000107/1 and British Antarctic Survey (BAS) capital funding. The radar frame design and construction were led by former BAS engineer Nic Mounteney. The Himalayan Research Expedition (P) Ltd. provided the field logistics.

References

Earthstar Geographics. (Undated). "World Imagery." Maps throughout this book were created using ArcGIS® software by Esri. ArcGIS® and ArcMap™ are the intellectual property of Esri and are used herein under license. Copyright © Esri. All rights reserved. For more information about Esri® software, please visit www.esri.com. Retrieved 15 April, 2025, from https://www.arcgis.com/home/item.html?id=10df2279f9684e4a9f6a7f08febac2a9.

Farinotti, D., D. J. Brinkerhoff, J. J. Fürst, P. Gantayat, F. Gillet-Chaulet, M. Huss, P. W. Leclercq, H. Maurer, M. Morlighem, A. Pandit, A. Rabatel, R. Ramsankaran, T. J. Reerink, E. Robo, E. Rouges, E. Tamre, W. J. J. van Pelt, M. A. Werder, M. F. Azam, H. Li and L. M. Andreassen (2021). "Results from the Ice Thickness Models Intercomparison eXperiment Phase 2 (ITMIX2)." Frontiers in Earth Science **8**.

Farinotti, D., M. Huss, J. J. Fürst, J. Landmann, H. Machguth, F. Maussion and A. Pandit (2019). "A consensus estimate for the ice thickness distribution of all glaciers on Earth." Nature Geoscience **12**(3): 168-173.

Frey, H., H. Machguth, M. Huss, C. Huggel, S. Bajracharya, T. Bolch, A. Kulkarni, A. Linsbauer, N. Salzmann and M. Stoffel (2014). "Estimating the volume of glaciers in the Himalayan–Karakoram region using different methods." The Cryosphere **8**(6): 2313-2333.

Gades, A. M., H. Conway and N. Nereson (2000). Radio echo-sounding through supraglacial debris on Lirung and Khumbu Glaciers, Nepal Himalayas. Debris-Covered Glaciers, Washington, USA, IAHS.

Gardner, A., M. Fahnestock and T. Scambos (2022). MEaSUREs ITS_LIVE Regional Glacier and Ice Sheet Surface Velocities, Version 1, NASA National Snow and Ice Data Center Distributed Active Archive Center.

GlaThiDa Consortium. (2020). "Glacier Thickness Database 3.1.0. World Glacier Monitoring Service." from https://www.gtn-g.ch/glathida/.

Huss, M. and D. Farinotti (2012). "Distributed ice thickness and volume of all glaciers around the globe." Journal of Geophysical Research: Earth Surface **117**(F4).

Jarvis, A., H. I. Reuter, A. Nelson and E. Guevara. (2008). "Hole-filled SRTM for the globe Version 4,." from http://srtm.csi.cgiar.org.

Jouvet, G. and G. Cordonnier (2023). "Ice-flow model emulator based on physics-informed deep learning." Journal of Glaciology **69**(278): 1941-1955.

King, E. C. (2020). "The precision of radar-derived subglacial bed topography: a case study from Pine Island Glacier, Antarctica." Annals of Glaciology **61**(81): 154-161.

King, O., D. J. Quincey, J. L. Carrivick and A. V. Rowan (2017). "Spatial variability in mass loss of glaciers in the Everest region, central Himalayas, between 2000 and 2015." The Cryosphere **11**(1): 407-426.

Li, F., F. Maussion, G. Wu, W. Chen, Z. Yu, Y. Li and G. Liu (2023). "Influence of glacier inventories on ice thickness estimates and future glacier change projections in the Tian Shan range, Central Asia." Journal of Glaciology **69**(274): 266-280.

Macheret, Y. Y., M. Y. Moskalevsky and E. V. Vasilenko (1993). "Velocity of radio waves in glaciers as an indicator of their hydrothermal state, structure and regime." Journal of Glaciology **39**(132): 373-384.

Marzeion, B., R. Hock, B. Anderson, A. Bliss, N. Champollion, K. Fujita, M. Huss, W. W. Immerzeel, P. Kraaijenbrink, J.-H. Malles, F. Maussion, V. Radić, D. R. Rounce, A. Sakai, S. Shannon, R. van de Wal and H. Zekollari (2020). "Partitioning the Uncertainty of Ensemble Projections of Global Glacier Mass Change." Earth's Future **8**(7): e2019EF001470.

Maurer, J. M., J. M. Schaefer, S. Rupper and A. Corley (2019). "Acceleration of ice loss across the Himalayas over the past 40 years." Science Advances **5**(6): eaav7266.

Maussion, F., A. Butenko, N. Champollion, M. Dusch, J. Eis, K. Fourteau, P. Gregor, A. H. Jarosch, J. Landmann, F. Oesterle, B. Recinos, T. Rothenpieler, A. Vlug, C. T. Wild and B. Marzeion (2019). "The Open Global Glacier Model (OGGM) v1.1." Geosci. Model Dev. **12**(3): 909-931.

Millan, R., J. Mouginot, A. Rabatel and M. Morlighem (2022). "Ice velocity and thickness of the world's glaciers." Nature Geoscience **15**(2): 124-129.

Minnaert, M. (1941). "The reciprocity principle in lunar photometry." Astrophysical Journal **93**: 7.

Moribayashi, S. (1978). "Transverse Profiles of Khumbu Glacier Obtained by Gravity Observation <I>Glaciological Expedition of Nepal, Contribution No. 46</I>." Journal of the Japanese Society of Snow and Ice **40**(Special): 21-25.

Phong, B. T. (1998). Illumination for computer generated pictures. Seminal graphics: pioneering efforts that shaped the field, Volume 1, Association for Computing Machinery. **Volume 1:** 95–101.

Plewes, L. A. and B. Hubbard (2001). "A review of the use of radio-echo sounding in glaciology." Progress in Physical Geography **25**(2): 203-236.

Pritchard, H., E. King, D. J. Goodger, D. Boyle, D. Goldberg, B. Recinos and A. Orr (2025). Raw and processed helicopter-borne radio-echo sounding ice thickness data from the glaciers of the Khumbu Himal, Nepal (2019) (Version 1.0) [Data set]. NERC EDS UK Polar Data Centre.

Pritchard, H. D. (2019). "Asia's shrinking glaciers protect large populations from drought stress." Nature **569**(7758): 649-654.

Pritchard, H. D. (2021). "Global data gaps in our knowledge of the terrestrial cryosphere." Frontiers in Climate **3**: 51.

Pritchard, H. D., E. C. King, D. J. Goodger, M. McCarthy, C. Mayer and R. Kayastha (2020). "Towards Bedmap Himalayas: development of an airborne ice-sounding radar for glacier thickness surveys in High-Mountain Asia." Annals of Glaciology **61**(81): 35-45.

RGI Consortium (2017). Randolph Glacier Inventory – A Dataset of Global Glacier Outlines: Version 6.0: Technical Report. Colorado, USA, Global Land Ice Measurements from Space.

Rounce, D. R., R. Hock and D. E. Shean (2020). "Glacier Mass Change in High Mountain Asia Through 2100 Using the Open-Source Python Glacier Evolution Model (PyGEM)." Frontiers in Earth Science **Volume 7 - 2019**.

Rowan, A. and D. Egholm. (2021). "Simulated ice thickness, supraglacial debris thickness and subglacial topography for Khumbu Glacier, Nepal, using the iSOSIA ice-flow model - VERSION 2.0 (Version 2.0)." from https://doi.org/10.5285/f62a1b8a-5a4c-451a-8dfb-28600b4049e8.

Rowan, A. V., D. L. Egholm, D. J. Quincey, B. Hubbard, O. King, E. S. Miles, K. E. Miles and J. Hornsey (2021). "The Role of Differential Ablation and Dynamic Detachment in Driving Accelerating Mass Loss From a Debris-Covered Himalayan Glacier." Journal of Geophysical Research: Earth Surface **126**(9): e2020JF005761.

Shean, D. (2017). High Mountain Asia 8-meter DEM Mosaics Derived from Optical Imagery, Version 1, NASA National Snow and Ice Data Center Distributed Active Archive Center.